OPEN ACCESS

University of BRISTOL

Xie, W., Yang, F., Ding, L., & Scarpa, F. (2019). Predictive models and experiments for high-velocity and high-temperature impacts in Inconel-alloy panels. *Materials and Design*, *182*, [108032]. https://doi.org/10.1016/j.matdes.2019.108032

Publisher's PDF, also known as Version of record

License (if available):
CC BY

Link to published version (if available):
10.1016/j.matdes.2019.108032

Link to publication record in Explore Bristol Research
PDF-document

This is the final published version of the article (version of record). It first appeared online via Elsevier at https://doi.org/10.1016/j.matdes.2019.108032 . Please refer to any applicable terms of use of the publisher.

University of Bristol - Explore Bristol Research

General rights

This document is made available in accordance with publisher policies. Please cite only the published version using the reference above. Full terms of use are available:
http://www.bristol.ac.uk/pure/about/ebr-terms

Materials and Design 182 (2019) 108032

Contents lists available at ScienceDirect

Materials and Design

journal homepage: www.elsevier.com/locate/matdes

Predictive models and experiments for high-velocity and high-temperature impacts in Inconel-alloy panels

Weihua Xie [a,*], Fan Yang [a,1], Li Ding [b,2], Fabrizio Scarpa [c,3]

[a] Science and Technology on Advanced Composites in Special Environment Laboratory, Harbin Institute of Technology, Harbin 150080, PR China
[b] Shenzhen Academy of Aerospace, Keji South Ten Road 6, Shenzhen, 518057, PR China
[c] Aerospace Engineering, University of Bristol, Bristol BS8 1TR, UK

HIGHLIGHTS

- Impact tests in Inconel panels are performed with various impact velocities, incident angles and environmental temperatures.
- Test data extracted from open literature and this work are used to validate the finite element model proposed in this paper.
- Phenomenological analytical models combined with finite elements are also proposed to obtain ballistic limit equations.

GRAPHICAL ABSTRACT

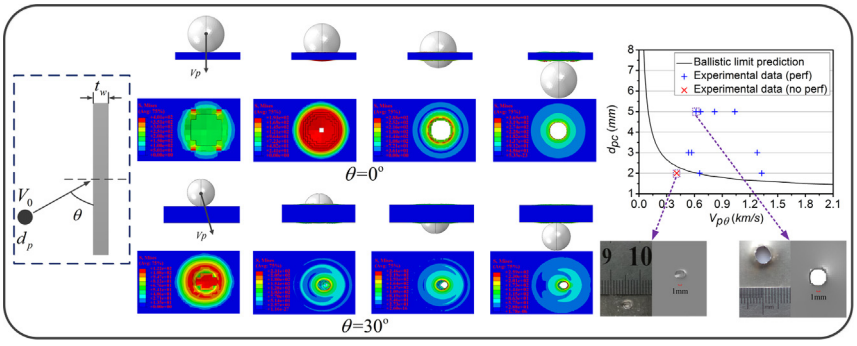

ARTICLE INFO

Article history:
Received 12 May 2019
Received in revised form 26 June 2019
Accepted 9 July 2019
Available online 10 July 2019

Keywords:
Inconel alloys
High velocity impact
High-temperature
Residual velocity
Ballistic limit

ABSTRACT

The behavior of Inconel 718 and 617 panels on the high-speed impact perforation mode at elevated temperatures and ballistic impact limit is here investigated using experimental and numerical methods. Impact tests have been performed using a custom-made two-stage light-gas gun rig, with the specimens being subjected to high temperatures (up to 1007 °C). The panels have been impacted using spherical projectiles with velocities ranging from 0.5 to 2.2 km/s. During the experiments the failure of the targets has been evaluated by varying parameters like the projectile diameter, its density and the oblique impact angle. An analytical model to estimate the residual velocity and the ballistic limit equations has been established. Finite element models (FEM) combined with phenomenological analytical models have been also developed to validate the predictive results obtained by the analytical model. The simulations from the FEM and the analytical models provide a good match with the experimental data. For the two typical cases (normal impact and oblique impact), the shapes and sizes of the damaged holes have been also well predicted by the numerical model. Equivalent diameters of the impacts have also been identified as functions of the velocity, diameter of the projectile and panel thickness.

© 2019 The Authors. Published by Elsevier Ltd. This is an open access article under the CC BY license (http://creativecommons.org/licenses/by/4.0/).

* Corresponding author at: Harbin Institute of Technology, No. 2 Yikuang Street, Harbin 150080, PR China.
E-mail address: michael@hit.edu.cn (W. Xie).
[1] Doctoral student, Harbin Institute of Technology, No.2 Yikuang Street, Harbin 150080, PR China.
[2] Doctor, Shenzhen Academy of Aerospace, Keji South Ten Road 6, Shenzhen, 518057, PR China.
[3] Professor, Bristol Composites Institute (ACCIS), University of Bristol, BS8 1TR Bristol, UK.

https://doi.org/10.1016/j.matdes.2019.108032
0264-1275/© 2019 The Authors. Published by Elsevier Ltd. This is an open access article under the CC BY license (http://creativecommons.org/licenses/by/4.0/).

Nomenclature

A	initial yield stress, MPa
A_h	hole area of the general impact, m^2
B	hardening constant
C	strain rate constant
d_p	projectile diameter, m
d_{pc}	critical diameter of the projectile for ballistic limit impact, m
d_h	equivalent hole diameter of the general impact, m
d_{ho}	square roots of longest and shortest ellipse diameter of the oblique impact, m
d_{hn}	actual hole diameter of the normal impact, m
m	thermal softening exponent
m_p	mass of the projectile, kg
m_b	mass of the plug moved out from the specimen, kg
n	hardening exponent
T	test temperature, °C
T_r	transition temperature, °C
T_m	melting temperature, °C
t_w	thickness of the specimen, m
V_0	initial velocity of the projectile, m/s
V_f	residual velocity of the projectile, m/s
V_p	impact velocity of the projectile, m/s
$V_{p\theta}$	normal component of impact velocity of the oblique impact, m/s
W_f	kinetic energy lost due to the inelastic impact of the projectile on the plug free of the surrounding material, J
W_s	energy lost during the penetration, J
x	forward distance along the direction of velocity, m
θ	impact angle, °
σ_w	dynamic yield shear strength of the specimen, MPa

1. Introduction

Inconel superalloys have been successfully used in the aeronautical [1–3], aerospace [4,5] and nuclear industry [6,7] due to their outstanding mechanic properties and corrosion resistance at elevated temperatures. The engineering applications in which Inconel superalloys structures are in general used involve the existence of a fracture or perforation threat and a strong thermally induced degradation [4,8,9].

A significant body of work concerning experimental and numerical analyses has been carried out to investigate the mechanical behavior and the dynamic failure mode of Inconel. Kajberg et al. [10] have developed three different modified fracture criteria to characterize and evaluate the mechanical behavior of Inconel 718 subjected to high strain rates ($1000s^{-1}$) and high temperature (650 °C) loadings. The criteria were verified with calibration experiments and the failure predictions were consistent with the real ones observed in the specimens. The effects of different strain rates on the performance of Inconel in hot environments have been evaluated by Lin [11], with a resulting modified constitutive model developed to characterize the hot deformation behavior of the 718 Alloy. The constitutive models of Inconel alloys are strain-rate dependent, and various experimental tests have also shown that the temperature is a non-negligible factor [12–14]. Split Hopkinson Pressure Bar (SHPB) tests have been used to investigate the failure and mechanical properties at high strain rates [15,16]. Lee and his team [17] have proposed an approach to evaluate the dynamic shear response and shear localization characteristics of Inconel 718 alloy at temperatures ranging from −150 °C to 550 °C. The microstructural evolution of the Inconel 718 subjected to high temperatures (950 °C to 1100 °C) and high strain rates (from 0.01 s^{-1} to 1 s^{-1}) have been also studied [18].

Several research teams have also focused on the ballistic impact response and failure mechanisms of metallic structures. Erice et al. [19] have performed a series of high-temperature ballistic impact experiments to obtain the mechanical behavior of Inconel 718. Mohotti [20] has investigated the ballistic limit curve for aluminum-polyurea composites subjected to relatively low velocity (945 m/s) impact loading, and an analytical model has also been developed to predict the residual velocity of the projectiles. A novel configuration for orbital debris shielding has been proposed by Huang [21], with a series of impact experiments also being conducted to evaluate the protection efficiency. A new metallic energy-absorbing bumper for vehicles has been successfully designed by Peng [22], and the crashworthiness of the structure has also been tested using both numerical and experimental techniques. The peak impact force and the penetration characteristics of Inconel 718 at high velocity impacts and an empirical ballistic limit curve have been derived by Di Sciuva et al. [23]. The impact response and the dynamic perforation mechanism of honeycomb sandwich panels have been extensively investigated by Sun [24]. The effects of the environmental temperature, impact velocity and their associated energy on the damage resistance of honeycomb sandwich and carbon carbon composites subjected to impacts have been studied systematically by Xie et al. [25,26].

Because the debris and dust does not always impact the shields along a perpendicular (normal) direction, the effect of the incident impact angle has also been systematically evaluated for space engineering [27,28]. Masahiro [29] have studied the size distribution of fragments in oblique impacts, and the results have revealed that size distributions and affected regions are strongly correlated to the strike angle. Tore et al. [30] have performed numerous normal and oblique impacts and found that 20 mm AA6082-T4 aluminum plates could not be perforated by the projectile when the incident angle exceeds 60°. Zhang et al. [31] have also studied the effects of impact angles and velocities on the perforation behavior of carbon fiber reinforced plastics, and the fracture patterns due to delamination and perforation have also been investigated.

This paper presents an experimental and analytical study of the effects of high velocity impacts (554 m/s to 2200 m/s) on Inconel718 and Inconel617 panels at temperatures of 25 °C, 450 °C, 700 °C and 1000 °C/1007 °C. The experimental tests were performed using a custom-made facility. An analytical model that describes the impact on the plates is developed. The model allows predicting the residual velocity and the ballistic limit equations for the impact case. Impact responses have also been numerically investigated with an ABAQUS/Explicit Finite Element model. The performance of the plates under oblique impacts is also investigated to consider some realistic loading situations, like space debris impact. To the best of the Authors' knowledge there is significant scarcity of data and models available in open literature about the performance of Inconel alloy panels under oblique impacts, in particular when performed at high velocities and high temperatures above 1000 °C. The objective of this paper is to provide some general design guidelines for metallic thermal protection shields with the proposed models and experimental data.

2. Experimental investigation

2.1. Specimen preparation

The experimental specimens used in this paper have been made from Inconel alloys (Inconel718 and Inconel617 - Fig. 1). The diameters of the spherical projectiles were measured before the tests, with a maximum deviation between their values less than 0.1 mm. The dimensions of panels were determined to ensure a reliable connection with the customized test rig and enough room for the high-velocity oblique impact.

The geometric and material parameters considered in the experiments are illustrated in Tables 1 and 2. All the experimental tests have

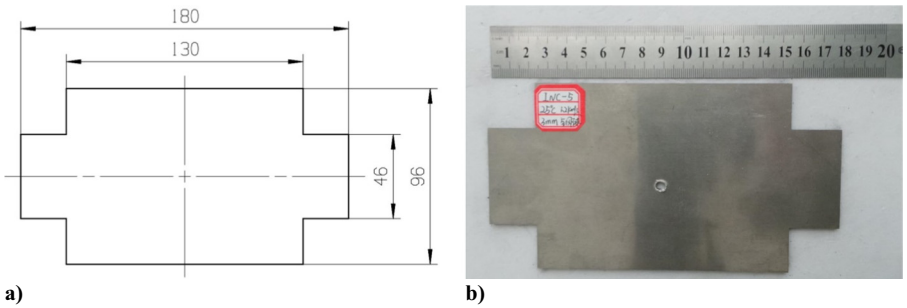

Fig. 1. Inconel Specimen (unit: mm): (a) dimension; (b) photo after impact INC-5.

been divided into two categories, i.e. the normal and the oblique impacts.

2.2. High temperature impact facilities set-up and test procedure

The impact facilities consist in a two-stage light-gas gun equipped with a fast electric heating system (Figs. 2 and 3). A custom-designed fast electric heating system is installed in the impact chamber to heat and also measure the temperatures of the specimens. To heat the samples, two ends of the specimens are first connected to a pair of copper electrodes that are then fixed to a supporting back plate (Fig. 2(b)). Voltage between 1 V and 4 V is applied at the two ends of the specimen via a transformer. Current between 10 A and 5000A is controlled, with the transient of the current causing a rapid temperature rising. A multi-wavelength pyrometer for a temperature higher than 299 °C (up to 3000 °C) has been used to measure and monitor the temperature of the specimens except for the ones subjected to room temperature (RT). The pressure of the chamber is kept at atmospheric levels during the tests.

The ballistic performance of the specimens is evaluated through normal and oblique impacts with velocities from 554 m/s to 2200 m/s. Fig. 4 shows a general sketch of the impact test performed. The projectiles are made of stainless steel, ZrO_2 and Si_3N_4 because of the outstanding hardness and toughness of those materials. Spherical projectiles with different diameters have been accelerated to the pre-determined velocity to impact the center of the targets with four incident angels (0°, 15°, 30° and 45°). The temperatures during the impact tests were kept under control at about 25 °C (RT), 450 °C, 700 °C and 1000 °C/1007 °C.

2.3. Impact test results

Eighteen high-velocity impact experiments have been performed. Only two plates have been completely destroyed, and no geometric deformation of the projectiles has also been observed at the same time. Circular holes were presented after the normal impact tests, while the plates subjected to oblique impact have shown holes with elliptical shapes (Fig. 13). The topologies of the holes have been evaluated by measuring the size of the damage holes. Tables 1 and 2 present a summary of the two test cases considered in this work. The thickness of the high-velocity impacts targets is relative small; that leads to the presence of holes with similar dimensions between the front and the back surfaces, with a mean deviation lower than 5%. The data contained in

Table 1
Oblique impact test results.

No.	d_p (mm)	Projectile material	θ (°)	Plate material	t_w (mm)	v_0 (m/s)	T (°C)	Test result*	Elliptical hole dimension#	
									a (mm)	b (mm)
INC-1	2	Steel	45	Inconel718	1.8	577	RT	No Perf	–	–
INC-2	2	Steel	30	Inconel718	1.8	758	453	Perf	2.62	2.35
INC-3	2	Steel	15	Inconel718	1.8	1374	704	Perf	3.54	3.2
INC-4	3	Steel	45	Inconel718	1.8	806	701	Perf	5.45	3.8
INC-5	3	Steel	30	Inconel718	1.8	1477	RT	Perf	5.78	4.67
INC-6	3	Steel	15	Inconel718	1.8	554	470	Perf	3.35	3.17
INC-7	5	Steel	45	Inconel718	1.8	1466	450	Perf	10.16	8.05
INC-8	5	Steel	30	Inconel718	1.8	945	719	Perf	8.05	6.04
INC-9	5	Steel	15	Inconel718	1.8	690	RT	Perf	5.6	5.4
INC-10	5	Steel	15	Inconel718	1.8	639	RT	Perf	6.39	5.55

#a: ellipse length, b: elliptical short diameter.
* Perf: the specimen was perforated; No Perf: the specimen was not perforated.

Table 2
Normal impact test results.

No.	d_p (mm)	Projectile material	θ (°)	Plate material	t_w (mm)	v_0 (m/s)	T (°C)	Test result	Hole diameter (mm)
G1	1	Si_3N_4	0	Inconel617	1	1796	RT	Perf	1.21
G2	3	Si_3N_4	0	Inconel617	1	1700	1000	Perf	5.5
G3	5	Si_3N_4	0	Inconel617	1	1790	1007	Perf	7.12
G4	5	Si_3N_4	0	Inconel617	1	1720	RT	Perf	6.43
G5	5	Si_3N_4	0	Inconel617	1	2200	1000	Perf	8.21
G6	5	Si_3N_4	0	Inconel617	1	1160	1000	Perf	6.15
G7	5	ZrO_2	0	Inconel617	1	1830	1000	Perf	9.62
G8	5	steel	0	Inconel617	1	1900	1000	Perf	7.56

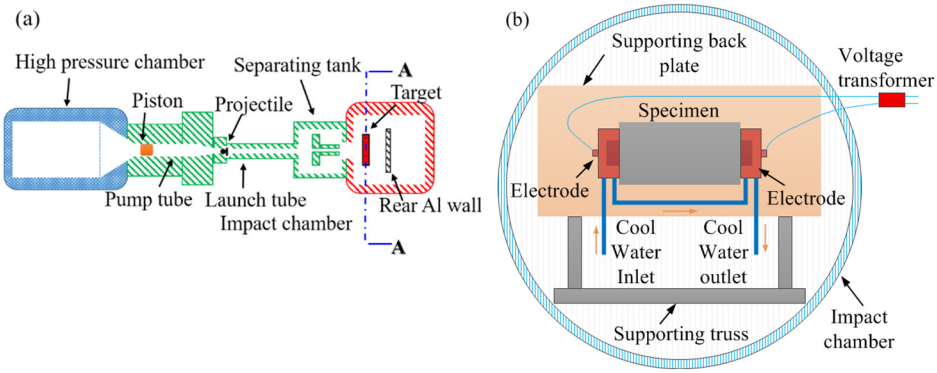

Fig. 2. Schematics of the impact facilities: a) two-stage light gas gun; b) impact setup in light gas gun impact chamber.

Tables 1 and 2 represent the average between the front and back surfaces.

Inconel718 panels with thickness of 1.8 mm have been used as target in ten oblique impact experiments. The impact energy of the INC-1 sample (about 5.4 J) was almost completely absorbed by the panel, and no perforation was observed on its back side. The impact energy carried by the projectile increases with the increase of its diameter and the initial velocity. As a consequence, the INC-7 sample with a projectile of velocity of 1.47 km/s and a diameter of 5 mm showed the largest damage area. Although the diameter of the projectile of the INC-3 test was smaller than the one related to the INC-6 impact, the INC-3 plate still exhibited a relatively large perforated hole area because of the higher impact velocity. For a constant projectile diameter, the tangential component of the velocity plays a significant role in the oblique impact tests, therefore so the values of the longest and shortest ellipse axis of the holes were different for the various impacts. The INC-9 and INC-10 tests were carried out in the same conditions (temperature, impact angle and diameter), however a larger damage area was observed in the INC-10 plate. The lower the velocity of the projectile, the rougher the edge around the hole would appear. An expanding shape was also observed in the back side of the INC-10 target.

The normal impact experiments have been performed with the 1 mm-thick Inconel617 panels. During two experiments (G3 and G4) the specimens have been hit by projectiles with diameter of 5 mm at constant impact velocity (about 1.7 km/s). The strength of the specimens at high temperature has shown a dramatic reduction compared to the room temperature case; the G3 sample therefore featured a larger circular damage hole at over 1000 °C, in comparison with the G4 specimen.

In summary, a multiple parameters test campaign has been used during the experimental investigations. The impact energy carried by the projectile has affected the dimensions of the damage section. No obvious wrinkles and deformations in the area surrounding the perforation have been observed. The holes featured the same shape on the front and back sides of the plates.

3. Analytical model

High velocity impacts can be divided into three different categories: within the ballistic, the shattered and vaporized ranges [32]. In this paper the metal panels experienced ballistic range impacts. Studies concerning the perforation modes of metal specimens within the ballistic range impact have been described in a very limited number of papers so far [32,33]. In those works the three velocity impact regimes have been differentiated by observing the features of the damaged targets. At low velocities impact (ballistic regime) the projectile tends to hit the target and bounces off leaving a local dent on the front side of the panels. The shattered regime has been characterized by the state of the back surface, with a perforation that tends to become dominated by an out-diffusion shape. The third regime (vaporized range) is characterized by a compression/shear failure of the target, and the type of perforation mode turns into a plug-shaped formation. The Inconel alloys plates tested at high velocity and temperature in this work feature perforations dominated by the formation of shaped plugs. The inside section around the holes of the perforated plates in this work appear

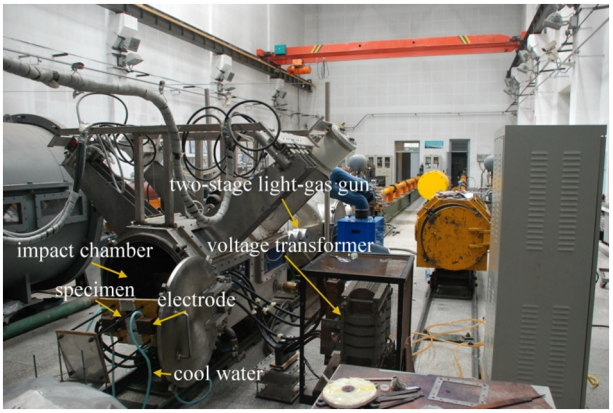

Fig. 3. Experimental setup.

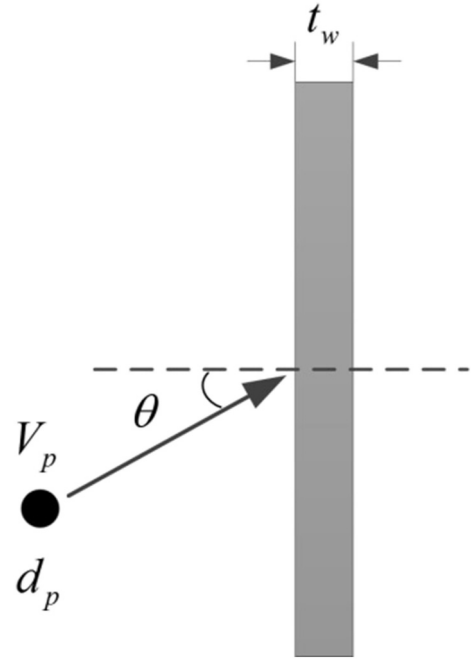

Fig. 4. Schematic of the impact.

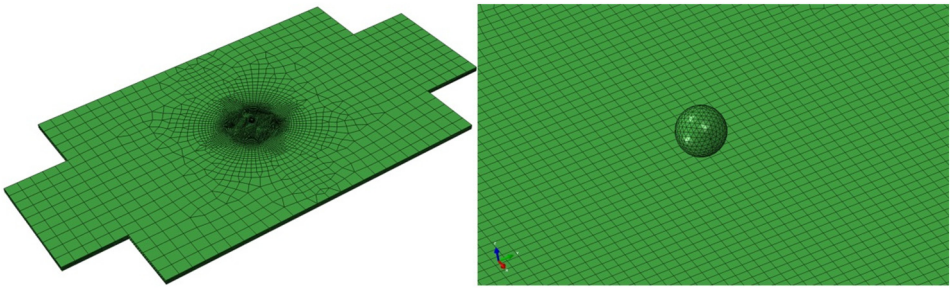

Fig. 5. Finite element model.

smooth, and therefore one could conclude that the portion of the specimen perforated is sheared by the projectile. The projectiles were also intact after the tests.

The residual velocity and the ballistic limit equations are important metrics and tools to design metallic thermal protection systems; the residual velocity is indicative of the protective capacity of the system, while the ballistic limit equations provide useful guidelines at the initial design stage.

The analytical model is based on the presence of an ideal spherical projectile that carries kinetic energy and hits the specimen at an impact angle. The perforated section of the target is removed by the shear force generated along the incident direction. The overall impact process assumes that the local energy dissipation is neglected, and the projectile plus the specimen debris travel with the same velocity after the impact. The equation that governs the conservation of energy can be formulated as:

$$m_p V_p^2/2 = (m_p + m_b)V_f^2/2 + W_s + W_f \tag{1}$$

As a simplification one can assume that the resistance acting on the projectile and the plug when they move forward relative to the surrounding plate material is mainly constituted by shearing forces [34]. The work W_s has therefore the following expression:

$$W_s = \int_0^{\frac{t_w}{\cos\theta}} A_h \sigma_w \left(\frac{t_w}{\cos\theta} - x\right) dx = \frac{\pi d_h t_w^2 \sigma_w}{2\cos^2\theta} \tag{2}$$

The term W_f can be estimated by momentum and energy considerations along the normal direction [35], i.e. $W_f = m_p m_b V_p^2/2(m_p + m_b)$. One then obtains:

$$\frac{m_p V_p^2}{2} = \frac{(m_p + m_b)V_f^2}{2} + \frac{\pi d_h t_w^2 \sigma_w}{2\cos^2\theta} + \frac{m_p m_b V_p{}^2}{2(m_p + m_b)} \tag{3}$$

The residual velocity V_f can therefore be derived as:

$$V_f = \left[\frac{m_p{}^2 V_p^2}{(m_p + m_b)^2} - \frac{\pi d_h t_w^2 \sigma_w}{(m_p + m_b)\cos^2\theta}\right]^{\frac{1}{2}} \tag{4}$$

The ballistic limit state can be defined as the zero residual velocity ($V_f = 0$). The ballistic limit equation is therefore:

$$m_p{}^2 (V_p \cos\theta)^2 = \pi d_h t_w^2 \sigma_w (m_p + m_b) \tag{5}$$

Common integral formulas can be applied to deduct the terms $m_p = \pi d_p^3 \rho_p/6$ and $m_w = \pi d_h^2 t_w \rho_w/4$ used in this paper. Taking the two expressions into Eqs. (4) and (5), the residual velocity and the ballistic limit equation can then be simplified as follows:

$$V_f = \left[\frac{d_p{}^6 \rho_p{}^2 V_p^2}{\left(d_p{}^3 \rho_p + 1.5 d_h{}^2 \rho_w t_w\right)^2} - \frac{6 d_h t_w^2 \sigma_w}{\left(d_p{}^3 \rho_p + 1.5 d_h{}^2 \rho_w t_w\right)\cos^2\theta}\right]^{\frac{1}{2}} \tag{6}$$

$$d_{pc}^6 \rho_p^2 (V_p \cos\theta)^2 = 6 d_{pc}^3 \rho_p \sigma_w t_w^2 d_h + 9 \rho_w \sigma_w t_w{}^3 d_h{}^3 \tag{7}$$

The analytical model is valid for thin target panels of isotropic materials and for cases in which the deflection of the velocity caused by the thin panel can be ignored.

4. Numerical simulations

4.1. Finite element modeling

The explicit Finite Element code ABAQUS (version 6.13) has been used for the numerical analysis. The FE model of the Inconel plates is shown in Fig. 5. The temperature-dependent mechanical and the material properties of the materials used in the simulation (Inconel alloys, steel, Si_3N_4 and ZrO_2) are described in Table 3.

The mesh density around the contact region and within a radius of ten millimeters has been increased to provide a more accurate prediction of the impact response close to the target. Before carrying the explicit analysis, mesh size and density, maximum time increment and element type of the FE model have been evaluated (see Table 4 and Fig. 6). Since the spherical projectiles used during the tests showed no visible deformation, the projectile has been modelled here as a rigid body.

The general contact algorithm [36] has been adopted to model the surface erosion on the target during the high-velocity impact, with the self-contact algorithm of the target being activated during the simula-

Table 3
Material properties of simulations.

Material	Target					Projectile		
	Inconel617		Inconel718			Steel	Si_3N_4	ZrO_2
Temperature (°C)	25	1000	25	400–500	700–800	25–1000	25–1000	25–1000
Density (g/cm^3)	8.36	8.36	8.22	8.22	8.22	7.85	3.44	6.0
Elastic modulus (GPa)	211	139	208	186	162			
Yield strength (MPa)	319	63	1172	1076	689			
Tensile strength (MPa)	769	96	1407	1317	758			

Table 4
Mesh details of the FE model.

Part	Element type	Mesh size (mm)	Number of elements
Projectile	C3D4	(rigid body)	6870
Inconel718	C3D8R	0.25*0.25*0.25	59,570
Inconel617	C3D8R	0.25*0.25*0.25	33,984

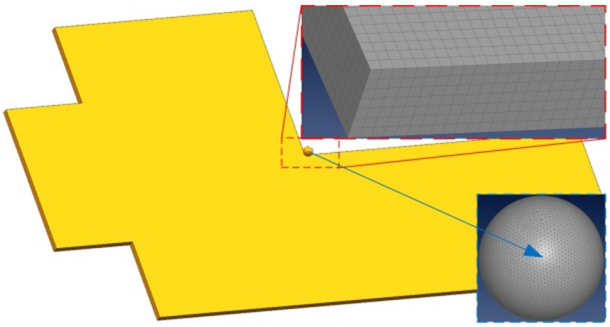

Fig. 6. Mesh detail of the model – test INC-10.

Table 5
Constitutive relation.[a]

Part	B (MPa)	n	C	m	$\dot{\varepsilon}(s^{-1})$	T_r(°C)	T_m(°C)
Inconel_718	1284	0.54	0.006	1.20	1e-3	25	1800
Inconel_617	1750	0.65	0.017	1.20	1e-3	25	1800

[a] Parameter A (initial yield stress at different temperatures) were listed in Table 3.

Table 6
Failure criteria.

D_1	D_2	D_3	D_4	D_5
0.04	0.75	−1.45	0.04	0.89

tion. Normal and tangential contact behavior has also been included. The hard contact model has been employed to define the normal behavior in all the cases, while for the oblique impact cases the static-kinetic exponential decay algorithm has been adopted to define the tangential behavior (static and kinetic coefficients of 0.27 and 0.16 [24]). The projectile had a predefined velocity field at the initial step of the simulation. The fixtures present in the tests have been represented by full clamps (zeroing all the nodal DOFs) at the two sides of the target. The high strain-rate behavior of the plastic metal has been represented by the Johnson–Cook (J-C) model [14,37,38]. The constitutive laws can be defined as a function of the yield stress and the effects of the strain rate, strain hardening and thermal softening [38,39]:

$$\sigma_{eq} = \left[A + B\varepsilon_{eq}^{n}\right]\left[1 + C\ \ln\dot{\varepsilon}_{eq}^{*}\right]\left(1 - T^{*m}\right) \tag{8}$$

$$\varepsilon_f = [D_1 + D_2\ \exp(D_3\sigma^*)]\left(1 + D_4\ \ln\dot{\varepsilon}_{eq}^{*}\right)(1 + D_5 T^*) \tag{9}$$

Equations [14,40,41] contain J-C parameters identified experimentally. To this end, the data from reference [42] have been used in this paper. Tables 5 and 6 list the J-C constitutive relation and the J-C failure criteria input parameters for the Inconel alloys. All the simulations have been implemented by the ABAQUS/Explicit solver which was installed on the workstation with 64GB RAM.

4.2. Validation of the FE model

Experimental results from open literature related to light gas gun tests [19] have been used first to verify the validity of the proposed numerical model. Erice et al. [19] have performed high velocity impacts on Inconel718 samples within a temperature range between 25 and 700 °C. The numerical solutions provided by the presently developed model are compared against the experimental results in [19] (Figs. 7 and 8). The FE model established in this paper provides an accurate prediction of the residual velocities and shape of the panels. The maximum deviation of the residual velocity from the experimental data does not exceed 11.2%.

The proposed FE model has been also validated by comparing the numerical predictions against the experimental results carried out in the present work. As listed in Table 7, the relative error of the damage area ranged from ~0% to 17.4%.

Figs. 9 and 10 show the general failure mechanism of the metallic specimens subjected to normal and oblique impact loading. The von-Mises stress distributions of the target at the moment of the impact are illustrated in Figs. 9(a) and 10(a). As the impact progresses on, the local stresses around the impacted section exceed the ultimate strength of the alloys; the material yields first and then cracks. Finally, the eroded elements are removed (Figs. 9–10(b), (c) and (d)). As the applied force is perpendicular to the target, the transient stress distribution is almost symmetrical during the normal impact. During oblique impacts, however, the transverse impact component tends to produce an additional stress field and a transient stress distribution combined with the one induced by the normal impact. The effect of the lateral velocity of the projectile modifies the contact region and creates an ellipse-shaped damage zone.

The impact responses predicted by the numerical results have been compared with the experimental results (Figs. 11–13). Shapes and sizes of the damaged zones described by the FE model appear to be quite consistent with the experimental data. The scale bars in the Figs. 11–13 are displayed in millimeters.

Plastic deformation will occur when the ductile panels are subjected to low strike velocity (Fig. 8). No apparent failure is observed after the impacts, and the projectile tends to rebound. When the impact velocity increases a local crater is left on the front side of the panels (Fig. 11). The plug-shaped deformation caused by the compression/shear failure in the panels will occur when the impact energy exceeds the strain energy associated to the resistance of the panel. Also, the higher impact energy

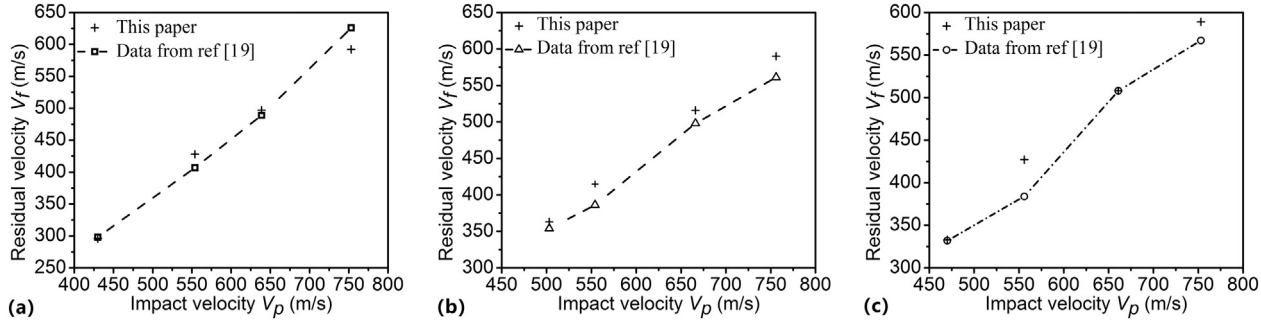

Fig. 7. Comparison of the residual velocities between the present model and experiments from open literature [19]: a) 25 °C; b) 400 °C; c) 700 °C.

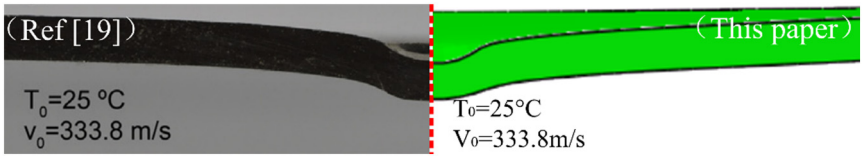

Fig. 8. Comparisons of the shape of non-perforated panels at room temperature provided by the current model and the experimental results in Ref. [19].

Table 7
Comparisons of damage area.

No.	Damage area from experiments (mm^2)	Damage area from simulation (mm^2)	Err%
INC-1	(No perf)	(No perf)	–
INC-2	4.84	5.68	17.36
INC-3	8.90	8.91	0.11
INC-4	16.27	17.18	5.60
INC-5	21.20	19.09	9.98
INC-6	8.34	7.63	8.47
INC-7	64.24	72.52	12.90
INC-8	38.19	40.08	4.95
INC-9	23.75	26.41	11.20
INC-10	27.85	28.06	0.75
G1	1.15	1.23	6.72
G2	23.76	25.50	7.32
G3	39.82	41.28	3.69
G4	32.47	35.78	10.20
G5	52.94	50.27	5.05
G6	29.71	25.52	14.10
G7	72.68	78.54	8.06
G8	44.89	41.28	8.03

the projectile carries, the smoother the perforation edge results (Figs. 12 and 13). The deformation in the damaged zone tends to be highly localized when the impact energy is increased [43,44].

5. Predictions and tests

The residual velocities and ballistic limit curves reflect the impact protection performance of metallic thermal protection shields (MTPS). This paragraph is dedicated to correlate those parameters to numerical and experimental results.

5.1. Residual velocity predictions and numerical simulations

The diameter of the perforation hole d_h is an essential parameter for the analytical expressions derived in Section 3. The validated FE model is applied to estimate an expression for d_h. Forty different numerical simulations have been carried out related to the two types of impact tests. The two cases have included normal velocities ranging from 200 m/s to 2000 m/s, and panel thickness varying between 0.5 mm and 2 mm. The environmental temperatures ranged from 25 °C (room

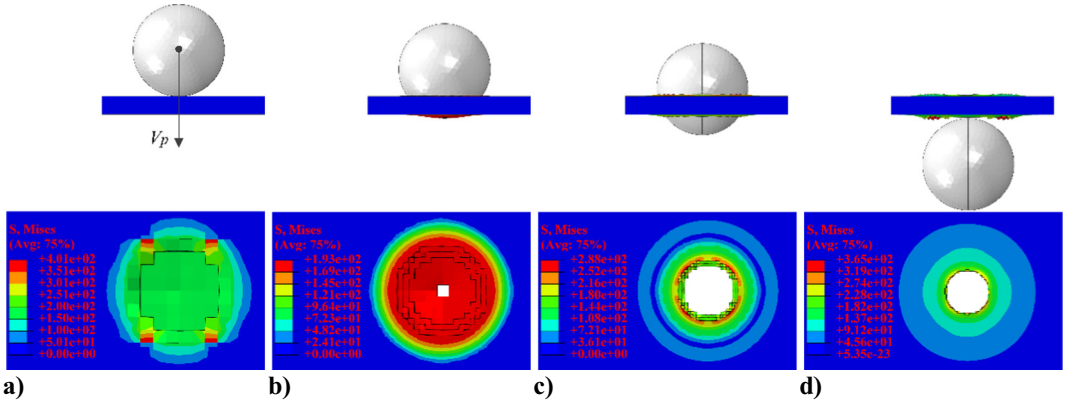

Fig. 9. Transient stress distribution during the normal impact under the G5 test conditions: a) initial contact; b) perforation started; c) projectile plugging; d) complete penetration.

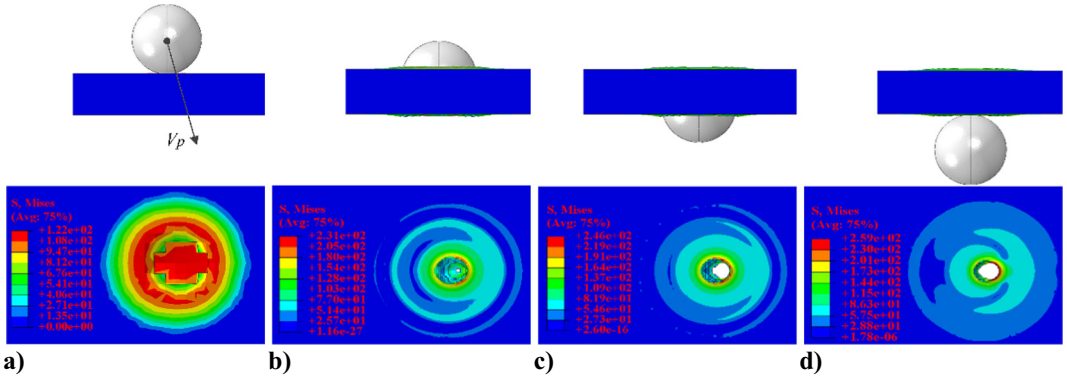

Fig. 10. Transient stress distribution during the oblique impact under the INC-5 test conditions: a) initial contact; b) perforation started; c) projectile plugging; d) complete penetration.

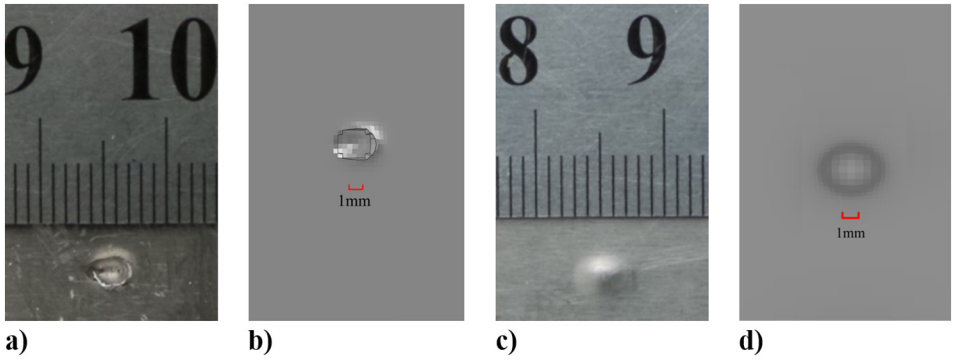

Fig. 11. Numerical and experimental results of the front and back surface - test INC-1: a) experimental result of the front surface; b) numerical result of the front surface; c) experimental result of the back surface; d) numerical results related to the back surface.

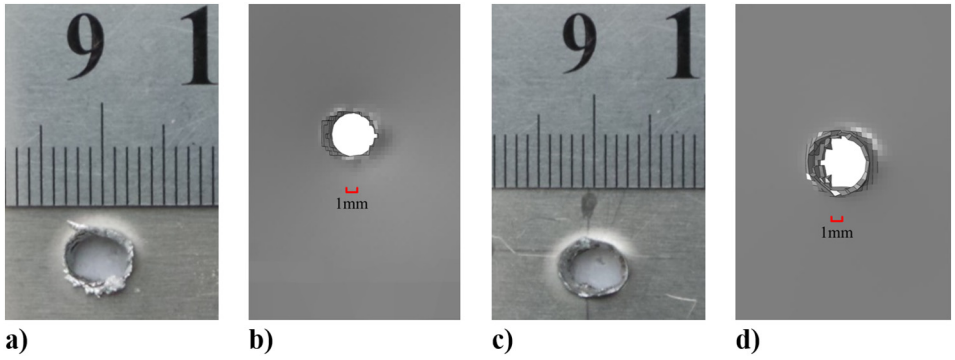

Fig. 12. Numerical and experimental results of the front and back surface - test INC-5: a) experimental result of the front surface; b) numerical result of the front surface; c) experimental result of the back surface; d) numerical result related to the back surface.

temperature) to 1000 °C. Three impact angles (15°, 30° and 45°) have been considered in the oblique impact case. The diameter d_h can be expressed as an exponential function of d_p, θ, V_p and t_w. All the numerical results have been fitted adopting a multiple nonlinear regression. The expressions of the equivalent diameter are:

$$d_{ho} = 3.8530 d_p \left(\frac{V_p \cos\theta}{c_w}\right)^{0.5199} \left(\frac{t_w}{d_p}\right)^{-0.1049} \quad R^2 = 0.9223 \tag{10}$$

$$d_{hn} = 3.3933 d_p \left(\frac{V_p}{c_w}\right)^{0.6304} \left(\frac{t_w}{d_p}\right)^{0.0214} \quad R^2 = 0.9175 \tag{11}$$

In the equations, $c_w = 5699.76$ m/s is the speed of sound in Inconel alloys [45].

Fig. 14(a) and (b) shows the residual velocities obtained by the FE simulations and the analytical predictions versus the impact velocity for the two impact cases. The comparison between the analytical and the numerical results shows a general good agreement.

The predictions related to the residual velocity show a general good agreement with the simulation results. For the particular conditions considered, the effect of shattered and scattered metallic debris may not be ignored. This is particularly true when the impact velocity exceeds 1 km/s and the residual energy cannot be completely absorbed by all the shattered debris, something that has been also observed during other experiments [46]. In addition, data related to the effective yield shear strength of the alloy during the dynamic loading are very limited in open literatures, therefore the quasi-static shear strength at room temperature is used here to calculate energy lost W_s during the penetration. This provides some justifications for the

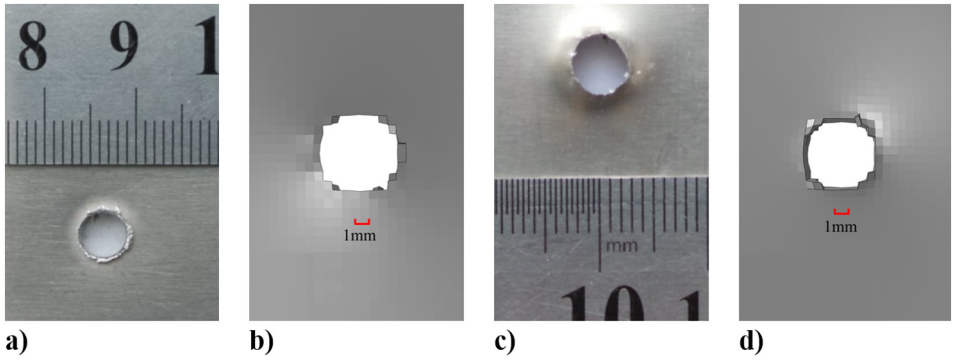

Fig. 13. Numerical and experimental results of the front and back surface - test INC-10: a) experimental result of the front surface; b) numerical result of the front surface; c) experimental result of the back surface; d) numerical results related to the back surface.

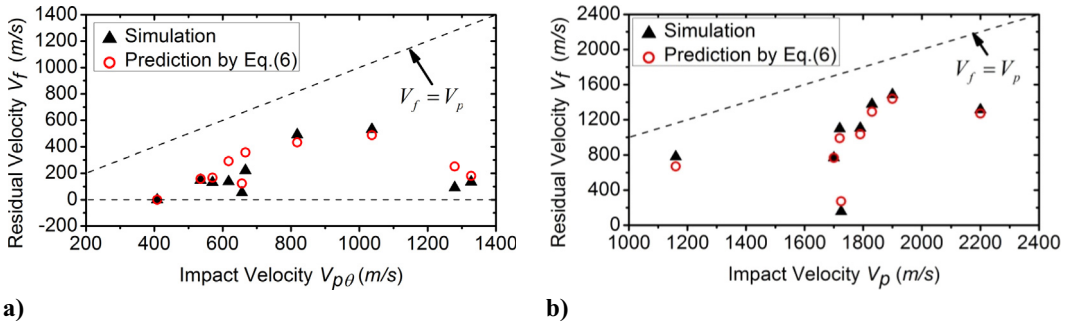

Fig. 14. Comparisons of analytical predictions and simulation of the residual velocity: a) oblique impact; b) normal impact.

difference in velocities between the numerical predictions and the theoretical results.

5.2. Ballistic limit curve prediction for the experimental tests

The diameter of the projectile diameter is here chosen as the critical parameter. Ballistic limit impact velocities lower than 3 km/s have been calculated by introducing Eqs. (10) and (11) into Eq. (7), and verified with the experimental results (Fig. 15). For the oblique impact case the impact velocity $V_p cos\theta$ is replaced with $V_{p\theta}$ in Eq. (7).

Fig. 15 shows the ballistic limit predictions for the four combinations of target and projectile considered in this work, with the points representing the experimental data. Single data located above the curve indicate that the target will be definitely perforated. The closer the point approaches to the curve, the lower the kinetic energy is after the impact. Data below the curve like in Fig. 15(a) indicate that no perforation will occur. All the experimental data obtained in this work (see Table 1) confirm the validity of the ballistic curves developed and their applicability to predict the general impact performance of Inconel alloy panels.

6. Conclusions

The behavior of Inconel plates under high-temperature high velocity impacts at elevated temperatures have been investigated in this paper. By using numerical and experimental methods, the impact resistance capacity of metallic panels and the ballistic limits performances have been evaluated. Experimental tests have been carried out in a custom two-stage light-gas gun rig, and an analytical model combined with a FE approach have also been established. Multivariate parameters such as temperature, impact velocity, impact angle, panel thickness and projectile diameter have been considered in these impact tests. The residual velocity and the ballistic limit equations for the different test cases have been identified. The main conclusions of the work are as follows:

Both normal and oblique impact cases showed one dominating perforation mode, i.e. the one related to combined compression and shear failure.

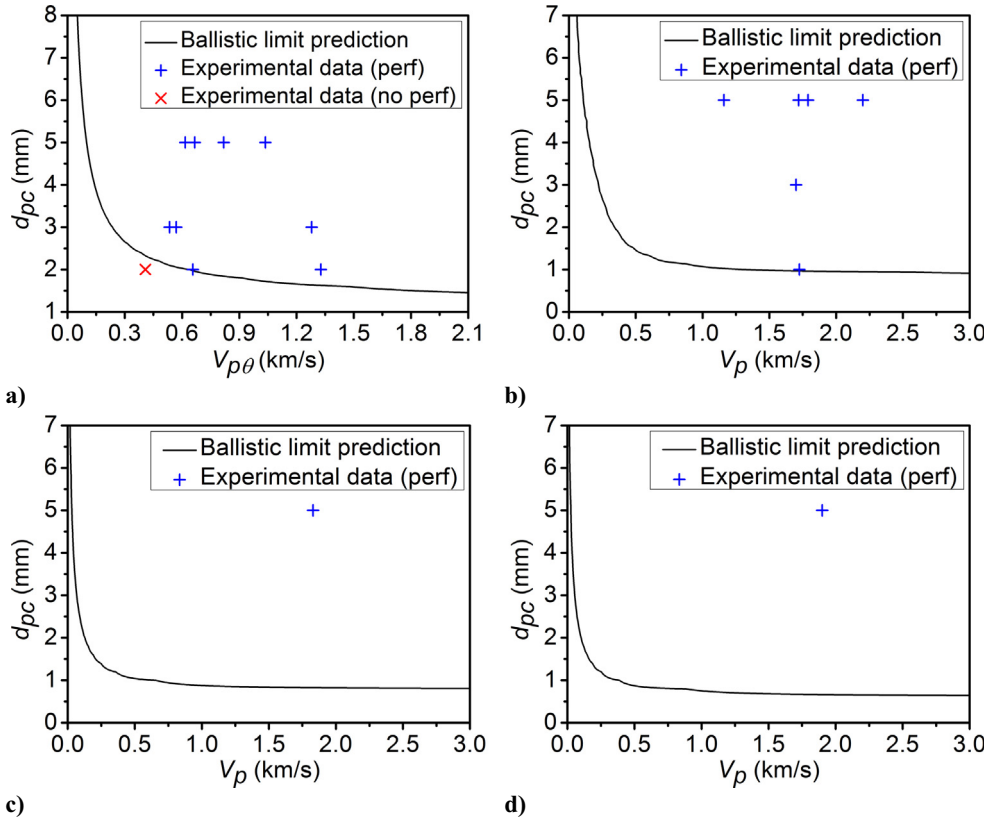

Fig. 15. Ballistic limit predictions and experimental data for different impacting pairs: a) Steel-Inconel718; b) Si3N4-Inconel617; c) ZrO2-Inconel617; d) Steel-Inconel617.

The analytical model developed is applicable to the plugged perforation mode. A phenomenological method was adopted to validate the FE model. The shape and geometry of the area of the holes obtained by the numerical model agrees well with tests results.

The residual velocity has been calculated using the analytical and numerical approaches. The results were in general good agreement, except for some particular cases. The ballistic limit curve developed to predict the impact resistance of the Inconel alloy plates has provided good results, with all the experimental data correctly predicted.

The proposed models and the experimental results can provide useful guidelines to design airframe and spaceframe MTPS that consider the effects of temperature, panel thickness, impact velocity, impact angle and projectile diameter on the performance of the target panels.

CRediT authorship contribution statement

Weihua Xie: Data curation; Investigation, Project administration, Resources, Supervision. **Fan Yang:** Formal analysis, Methodology, Software Writing-original draft. **Li Ding:** Validation, Visualization. **Fabrizio Scarpa:** Writing-review & editing.

Acknowledgements

This work has been supported by the Natural Science Foundation of China (11672088) and the National Basic Research Program of China (973 program) (No. 2015CB655200). In addition, authors want to thank Science & Technology on Reliability & Environmental Engineering Laboratory for the funding.

References

[1] J. Huebner, et al., Microstructure of laser cladded carbide reinforced Inconel 625 alloy for turbine blade application, Ceram. Int. 43 (12) (2017) 8677–8684.
[2] A. Chamanfar, et al., Microstructural characteristics of forged and heat treated Inconel-718 disks, Mater. Des. 52 (2013) 791–800.
[3] H.Y. Zhang, et al., Deformation characteristics of delta phase in the delta-processed Inconel 718 alloy, Mater. Charact. 61 (1) (2010) 49–53.
[4] J.C. Liou, N.L. Johnson, Planetary science. Risks in space from orbiting debris, Science 311 (5759) (2006) 340–341.
[5] R.P. Bernhard, E.L. Christiansen, D.E. Kessler, Orbital debris as detected on exposed spacecraft, International Journal of Impact Engineering 20 (1–5) (1997) 111–120.
[6] P. Berge, J.R. Donati, Materials requirements for pressurized water reactor steam generator tubing, Nucl. Technol. 55 (1) (1981) 88–104.
[7] M.S. Rahman, et al., Elevated temperature tribology of Ni alloys under helium environment for nuclear reactor applications, Tribol. Int. 123 (2018) 372–384.
[8] M. Cui, et al., Inverse analysis for simultaneously estimating multi-parameters of temperature-dependent thermal conductivities of an Inconel in a reusable metallic thermal protection system, Appl. Therm. Eng. 125 (2017) 480–488.
[9] R. Zhao, et al., Fracture behavior of Inconel 718 sheet in thermal-aided deformation considering grain size effect and strain rate influence, Mater. Des. 130 (2017) 413–425.
[10] T. Sjoberg, J. Kajberg, M. Oldenburg, Calibration and validation of three fracture criteria for alloy 718 subjected to high strain rates and elevated temperatures, European Journal of Mechanics A-Solids 71 (2018) 34–50.
[11] Y.C. Lin, et al., New constitutive model for high-temperature deformation behavior of inconel 718 superalloy, Mater. Des. 74 (2015) 108–118.
[12] K. Hazeli, et al., Microstructure-topology relationship effects on the quasi-static and dynamic behavior of additively manufactured lattice structures, Mater. Des. 176 (2019), 107826.
[13] M. Azarbarmas, et al., Microstructural evolution and constitutive equations of Inconel 718 alloy under quasi-static and quasi-dynamic conditions, Mater. Des. 94 (2016) 28–38.
[14] X. Wang, et al., Dynamic behavior and a modified Johnson–Cook constitutive model of Inconel 718 at high strain rate and elevated temperature, Mater. Sci. Eng. A 580 (2013) 385–390.
[15] G. Chen, et al., Temperature dependent work hardening in Ti-6Al-4V alloy over large temperature and strain rate ranges: experiments and constitutive modeling, Mater. Des. 83 (2015) 598–610.
[16] Z. Zhu, et al., Mechanical properties and dynamic constitutive model of 42CrMo steel, Mater. Des. 119 (2017) 171–179.
[17] W. Lee, et al., Dynamic mechanical behaviour and dislocation substructure evolution of Inconel 718 over wide temperature range, Materials Science and Engineering A-Structural Materials Properties Microstructure and Processing 528 (19–20) (2011) 6279–6286.
[18] N. Nayan, et al., Microstructure and micro-texture evolution during large strain deformation of Inconel alloy IN718, Mater. Charact. 110 (2015) 236–241.
[19] B. Erice, M.J. Perez-Martin, F. Galvez, An experimental and numerical study of ductile failure under quasi-static and impact loadings of Inconel 718 nickel-base superalloy, International Journal of Impact Engineering 69 (2014) 11–24.
[20] D. Mohotti, et al., Analytical and numerical investigation of polyurea layered aluminium plates subjected to high velocity projectile impact, Mater. Des. 82 (2015) 1–17.
[21] X. Huang, et al., Hypervelocity impact of TiB2-based composites as front bumpers for space shield applications, Mater. Des. 97 (2016) 473–482.
[22] P. Xu, et al., Cut-out grooves optimization to improve crashworthiness of a gradual energy-absorbing structure for subway vehicles, Mater. Des. 103 (2016) 132–143.
[23] . Di Sciuva, M., C. Frola and S. Salvano, Low and high velocity impact on Inconel 718 casting plates: ballistic limit and numerical correlation. International Journal of Impact Engineering, 2003. 28(8): p. 849–876.
[24] G. Sun, et al., High-velocity impact behaviour of aluminium honeycomb sandwich panels with different structural configurations, International Journal of Impact Engineering 122 (2018) 119–136.
[25] W.H. Xie, et al., High-temperature high-velocity impact on honeycomb sandwich panels, Composites Part B-Engineering 138 (2018) 1–11.
[26] W.H. Xie, et al., High velocity impact tests on high temperature carbon-carbon composites, Composites Part B-Engineering 98 (2016) 30–38.
[27] E.L. Christiansen, E. Cykowski, J. Ortega, Highy oblique impacts into thick and thin targets, International Journal of Impact Engineering 14 (1) (1993) 157–168.
[28] W.P. Schonberg, Characterizing secondary debris impact ejecta, International Journal of Impact Engineering 26 (1) (2001) 713–724.
[29] M. Nishida, K. Hayashi, K. Toya, Influence of impact angle on size distribution of fragments in hypervelocity impacts, International Journal of Impact Engineering 128 (2019) 86–93.
[30] T. Børvik, et al., Normal and oblique impact of small arms bullets on AA6082-T4 aluminium protective plates, International Journal of Impact Engineering 38 (7) (2011) 577–589.
[31] W. Xie, et al., Experimental investigation of normal and oblique impacts on CFRPs by high velocity steel sphere, Compos. Part B 99 (2016) 483–493.
[32] E.L. Christiansen, Design and performance equations for advanced meteoroid and debris shields, International Journal of Impact Engineering 14 (1–4) (1993) 145–156.
[33] E.L. Christiansen, K.J., ballistic limit equations for spacecraft shielding, International Journal of Impact Engineering 26 (2001) 93–104.
[34] L. Ding, et al., Ballistic limit equations in ballistic and shatter regions, International Journal of Impact Engineering 35 (12) (2008) 1490–1496.
[35] H.X. Zhu, N.J. Mills, The in-plane non-linear compression of regular honeycombs, Int. J. Solids Struct. 37 (13) (2000) 1931–1949.
[36] Version, 6.13. Analysis User's Manual. , Dassault Systemes Simulia Corp, Providence, RI, 2013.
[37] G.R. Johnson, W.H. Cook, Fracture characteristics of 3 metals subjected to various strains, strain rates, temperatures and pressures, Eng. Fract. Mech. 21 (1) (1985) 31–48.
[38] A. Iturbe, et al., Mechanical characterization and modelling of Inconel 718 material behavior for machining process assessment, Materials Science and Engineering A-Structural Materials Properties Microstructure and Processing 682 (2017) 441–453.
[39] J.J. DeMange, J.M. Pereira, B.A. Lerch, V. Prakash, Ballistic impact behavior of Ni-based super alloys with applications to engine fan-blade containment, Proceedings of the SEM IX International Congress on Experimental Mechanics, Society of Experimental Mechanics, Bethel, CT 2000, pp. 344–347.
[40] T. Ozel, Y.M. Arisoy, Experimental and numerical investigations on machining induced surface integrity in Inconel-100 Nickel-Base alloy, Procedia CIRP 13 (2014) 302–307.
[41] T. Ozel, et al., 3D finite element modelling of chip formation process for machining Inconel 718: comparison of FE software predictions, Mach. Sci. Technol. 15 (2011) 21–46.
[42] B. Erice, F. Galvez, A coupled elastoplastic-damage constitutive model with lode angle dependent failure criterion, Int. J. Solids Struct. 51 (1) (2014) 93–110.
[43] E.L. Christiansen, Design and performance equations for advanced meteoroid and debris shields, International Journal of Impact Engineering 14 (1) (1993) 145–156.
[44] T. Fras, C.C. Roth, D. Mohr, Dynamic perforation of ultra-hard high-strength armor steel: impact experiments and modeling, International Journal of Impact Engineering 131 (2019) 256–271.
[45] Ultrasonic Velocity of Materials, https://www.panamiris.com/downloads/UltrasoundVelocity.pdf.
[46] P.N. Verma, K.D. Dhote, Characterising primary fragment in debris cloud formed by hypervelocity impact of spherical stainless steel projectile on thin steel plate, International Journal of Impact Engineering 120 (2018) 118–125.